THE JOURNAL OF PHYSICAL CHEMISTRY C
A JOURNAL OF THE AMERICAN CHEMICAL SOCIETY

Open Access
This article is licensed under CC-BY 4.0

pubs.acs.org/JPCC
Article

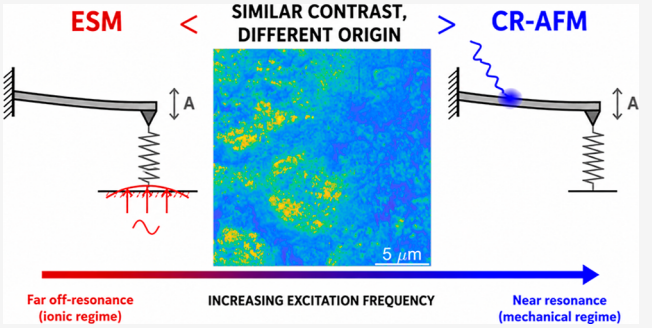
Revealing the Mechanical Contributions to the Signal Origin in Electrochemical Strain Microscopy

Niklas Scheer, Rüdiger-A. Eichel, and Florian Hausen*

Cite This: https://doi.org/10.1021/acs.jpcc.6c01404
Read Online

ACCESS | Metrics & More | Article Recommendations

ABSTRACT: Electrochemical strain microscopy (ESM) is typically applied to investigate local ionic motion by detecting surface displacement caused by an applied alternating current (AC) voltage. However, this displacement is not the only factor affecting the measured ESM signal. In this study, a strong correlation between ESM contrast and purely mechanical contrast obtained using contact resonance atomic force microscopy (CR-AFM) is demonstrated. This correlation suggests that additional nonionic mechanisms impact the ESM response. While ionic displacement typically occurs on a scale of a few pico-to nanometer and is most pronounced at low excitation frequencies, the results reveal enhanced contrast at higher frequencies, particularly when exciting the second eigenmode of the cantilever. Correlative measurements demonstrate that this contrast enhancement is present consistently in both ESM and CR-AFM data, suggesting that the mechanical properties of the tip−sample contact have a significant impact on the amplitude of the ESM signal. These findings emphasize the importance of considering mechanical contributions when interpreting ESM measurements, particularly at higher excitation frequencies.



Downloaded via RWTH AACHEN HOCHSCHUL BIBL on June 15, 2026 at 14:06:57 (UTC).
See https://pubs.acs.org/sharingguidelines for options on how to legitimately share published articles.

INTRODUCTION

Electrochemical strain microscopy (ESM) is a scanning probe technique that facilitates the identification of the local concentration and mobility of ions within a material.[1−7] Therefore, it is highly suited to study battery materials such as NCM ($LiNi_xCo_yMn_zO_2$ with x + y + z = 1).[8,9] However, ESM is also subject to imaging artifacts and the signal origin in ESM is currently discussed in the literature, given that various influences appear to play a significant role.[10] The initial explanation regarding the origin of the ESM signal has been the oscillation of ion concentrations in a locally applied alternating electrical field, that is applied to the stationary or scanning ESM probe in contact with the sample.[2,11,12] Due to the correlation between ion concentration and unit cell volume, known as Vegard strain, the field cycling invariably leads to the deformation of the sample, the magnitude of which is measured by the ESM probe. However, the possibility of further signal origins is addressed in recent publications. Badur et al. performed ESM measurements on a copper material with exceptionally high Vegard strain, concluding that Vegard strain and electrostatic contributions are in the same range.[13] Schön et al. and Lushta et al. also revealed the importance of electrostatic contributions to the ESM signal.[14,15] Further, Bradler et al. highlighted the influence of the tracking process on the ESM signal.[16] A summary of additional factors that may also exert an influence on the detected deflection signal of the cantilever, including, but not limited to, phase transitions, Joule heating, dipoles, charge injection and the field effect are provided in a recent opinion paper by Hausen and Balke.[10]

An additional parameter that does not necessarily align with the anticipated small deformation values associated with Li ions within the material but affects the ESM signal and has not been fully considered yet, is the role of local mechanical properties. In this paper, a correlative approach is adopted to investigate the influence of mechanics on the ESM signal. Consequently, two distinct AFM techniques namely ESM and contact resonance atomic force microscopy (CR-AFM) are employed.[17−22]

CR-AFM is a technique that measures the shift in the contact resonance frequency of an AFM cantilever in contact with a sample to map nanoscale mechanical properties such as stiffness and viscoelasticity. For contact resonance AFM, the cantilever is actively driven with photothermal excitation to vibrate always in contact with the surface. This leads to an oscillation of the cantilever, which is controlled by a phase-

Received: March 6, 2026
Revised: May 15, 2026
Accepted: May 18, 2026

ACS Publications
© XXXX The Authors. Published by American Chemical Society

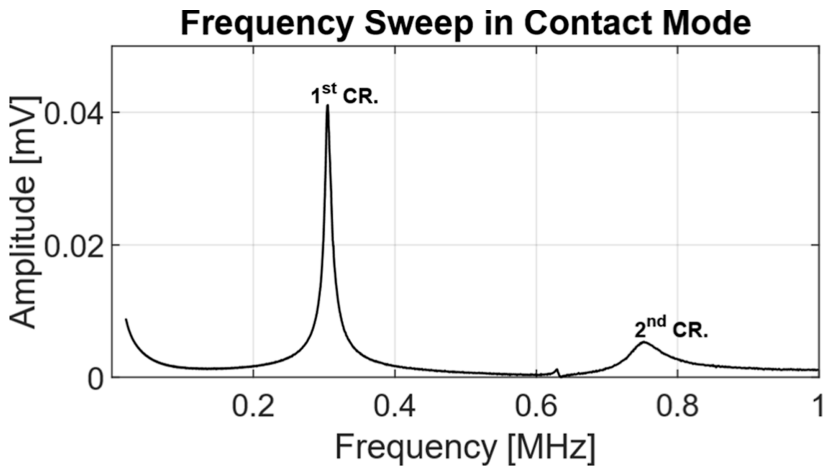


Figure 1. Frequency sweep of the in the publication used cantilever from 20 kHz−2 MHz in contact.

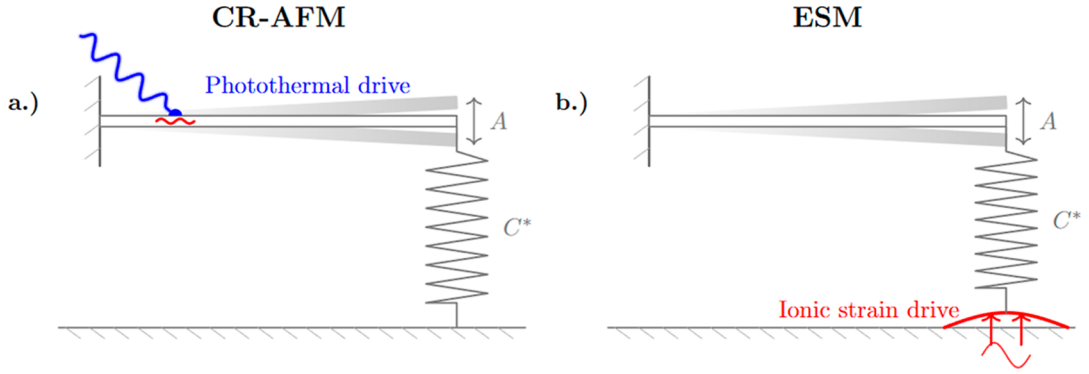


Figure 2. Schematic of the different excitation mechanism for (a) CR-AFM and (b) ESM.

locked loop (PLL) to achieve a driving frequency equal to the contact resonance.[23]

In ESM, the cantilever is also in contact with the surface but in contrast no direct external excitation for the cantilever is used, only an AC field is applied. The source of excitation is the ionic reorganization caused by this applied AC field resulting in an indirect excitation of the cantilever. This excitation allows the measurement of phase, amplitude and contact resonance.[24]

EXPERIMENTAL PART

The NCM622 sample, consisting of spherical particles with an average size of 100−250 nm, was synthesized in accordance with an established protocol by partners.[25] The sample consists of 92.5% cathode material, 4% Timcal Super C65, and 3.5% PVDF (Solef). The slurry was cast onto alumina foil and subsequently dried at 80 °C for a duration of 12 h. Subsequently, the specimen was positioned between two copper blocks to enhance the electronic conductivity and embedded in epoxy resin (EpoFix). The upper portion of the specimen was subsequently subjected to mechanical polishing in order to achieve a smooth surface. A multiscale characterization of the samples and images of the exact procedure of sample preparation including optical images of the sample itself as well as near edge X-ray absorption fine structure spectroscopy data, Conductive AFM images, and nanoindentation results are shown in the following publications.[8,9]

The AFM experiments were performed with a commercial AFM (Cypher, Asylum Research). The cantilevers employed in this study were conductive Pt/Ir EFM tips from Nanosensors, with a nominal force constant of 3 N/m and a free resonance frequency of 75 kHz. The photothermal excitation of the cantilever was performed using an HF2LI (Zurich Instruments), where only the control voltage of the laser was frequency adjusted, while the direct laser voltage itself remained unchanged, allowing the frequency adjustment of the excitation frequency. For the ESM measurements, an AC voltage of 8 V was applied, directly to the tip.

RESULTS AND DISCUSSION

Theoretical Considerations

The amplitude value of the ESM signal can be directly transferred to the deformation caused by ionic motion. The fundamental premise of this study is to consider mechanical contributions when interpreting ESM measurements, particularly at higher excitation frequencies. Figure 1 illustrates that the first contact resonance frequency is located at approximately 300 kHz, while the second is found significantly higher, around 750 kHz. Another designation for these are the eigenmodes of the cantilever. The first contact resonance manifests at a comparatively high amplitude. The subsequent peak, the lateral resonance frequency, is beyond the scope of this publication and is barely visible. The final peak, designated as 2. CR, exhibits a lower amplitude in comparison to the initial peak.

In contact resonance AFM, an external excitation is provided by laser excitation, therefore, the cantilever oscillates at the contact resonance frequency, causing an interaction with the sample. This excitation source is also located far away from the tip position of the cantilever, schematically shown in Figure 2. For ESM, however, the situation is different: oscillation of the tip is caused by ions oscillating under the tip, so the driving

https://doi.org/10.1021/acs.jpcc.6c01404
J. Phys. Chem. C XXXX, XXX, XXX−XXX

force is located directly under the tip and not at the beginning of the cantilever. If the frequency exceeds the maximum possible migration speed of the ions, the oscillation should stop. If there is still measurable oscillation, there must be another acting force that is not based on the ions. A clear separation of the excitation sources for the CR-AFM and ESM are given in Figure 2.

The interaction of the tip with the sample, and the resulting amplitudes for both cases, can be described by the following equations.

The amplitude response of an atomic force microscopy (AFM) cantilever in free oscillation is described by simple harmonic oscillator modes. Often this model is also used for describing nonfree oscillation like tapping, but this model neglects the tip−sample interaction. As this paper investigates this interaction, and the experiments are performed with constant contact between the tip and the sample, which plays an important role in CR-AFM[26,27] the model of a driven damped harmonic oscillator (DDHO) is used.[28,29] The equation of motion under external sinusoidal excitation yields a frequency-dependent amplitude[30]

$$A(f) = \frac{F_n}{\sqrt{(k_{\text{eff}} - m(2\pi f)^2)^2 + (2\pi f \cdot \gamma_n)^2}} \tag{1}$$

In eq 1 the amplitude is labeled A; the force is F_n (note: this is the oscillation force, not the static tip-force set point); the effective spring constant is k_{eff}; the frequency is f; the effective mass is m; and γ_n is the damping coefficient. All parameters are mode-dependent and are indexed by the mode number n. Equation 1 contains two parts that represent the sample interaction. In the DDHO model, forces and interactions are represented by springs. Consequently, the cantilever and the sample are both described by different spring constants. Combined, these form k_{eff}, which is split into $k_{cantilever}$ and k_{sample}. For a given set point and within the linear approximation, k_{sample} is treated as constant during the cantilever mode-dependent stiffness. The second interaction part is the damping coefficient γ, which includes contributions from the cantilever itself, the tip−sample interaction, and the environment. Under the assumption of a linearized effective contact stiffness, k_{eff} can be described by

$$k_{\text{eff}} = k_{\text{cantilever}} + k_{sample} \tag{2}$$

To maximize the amplitude, the denominator needs to be minimized. For a given damping coefficient, the amplitude is maximized when the stiffness and inertia terms cancel out. For light damping, the maximum amplitude is achieved when:

$$k_{\text{eff}} - m(2\pi f)^2 \approx 0 \Rightarrow \omega = 2\pi f = \omega_r \approx \sqrt{\frac{k_{\text{eff}}}{m}} \tag{3}$$

$$A(\omega_r) \approx \frac{F_n}{\omega_r \gamma_n} \propto \frac{1}{\sqrt{k_{\text{eff,n}}}} \tag{4}$$

Although an AFM cantilever is physically described as a continuous Euler−Bernoulli beam exhibiting an infinite number of flexural eigenmodes, the dynamic response in the vicinity of a resonance is dominated by a single mode. In this frequency range, the cantilever dynamics can therefore be approximated by a single-mode driven damped harmonic oscillator. Therefore, Equations 1−4 can be applied independently to each flexural mode, with parameters that depend on the mode: $k_{eff,n}$, γ_n, and F_n. This single-mode approximation is routinely used in AFM and is valid in the vicinity of each resonance peak, where the frequency response is dominated by a single modal contribution.[30−32]

In the case of splitting the analysis into CR-AFM for mechanical information and ESM for ionic information, the following assumptions can be made. In order to undertake the requisite resonance measurements, the equation must first be divided into two constituent cases. Equation 4 is generally valid for all kinds of dynamic measurements; the difference between CR-AFM and ESM is based on the excitation method. In CR-AFM, the cantilever is actuated through photothermal excitation, where periodic laser heating induces mechanical oscillation. The resulting amplitude $A_{pt,n}$ can therefore be described using the photothermal force $F_{pt,n}$.

$$A_{pt,n}(\omega_{r,n}) \approx \frac{F_{pt,n}}{(\omega_{r,n}\gamma_n)} \tag{5}$$

In contrast, the ESM signal is based on the displacement of the sample by ionic motion. The displacement u_{ion} can be described with the effective electrochemical strain coefficient or Vegard coefficient, denoted by α, which describes the displacement of the ions achieved per applied volt V_{ac}.[7]:

$$\mathrm{u}_{ion} \approx \alpha V_{ac} \tag{6}$$

The Vegard coefficient describes the coupling between changes in ionic concentration and the resulting lattice strain in a material, quantifying how strongly the lattice expands or contracts in response to compositional variations. In a strict sense, the Vegard coefficient itself is not a frequency dependent material constant, but rather reflects a quasi-static relationship. Any apparent frequency dependence of the measured deformation arises from kinetic limitations such as ionic diffusion and relaxation processes, which cannot follow at higher frequencies and therefore reduce the effective displacement. This implies that frequency dependent responses observed in ESM measurements are governed by transport dynamics rather than an intrinsic variation of the Vegard coupling. The ionically induced surface displacement act as a prescribed base excitation at the tip−sample contact and can therefore be represented by an equivalent modal force $F_{ion,n}$ within the linearized contact approximation.

$$F_{ion,n}(\omega) \approx k_{eff,n}\mathrm{u}_{ion}(\omega) \tag{7}$$

Analogous to eq 5, the amplitude $A_{ion,n}$ here can then be described in a form of:

$$A_{ion,n}(\omega_{r,n}) \approx \frac{k_{eff,n}\mathrm{u}_{ion}}{(\omega_{r,n}\gamma_n)} \tag{8}$$

The ionic motion induces a local lattice expansion described by the Vegard coefficient, which acts as a base excitation at the tip−sample contact. This excitation is converted into an effective modal force and amplified by the contact resonance, resulting in a measured amplitude that strongly depends on the mechanical properties of the system rather than purely on ionic effects. At the resonance frequency, an increase in the oscillation amplitude is expected according to eq 4. However, it is important to note that the measured amplitude values at resonance frequencies do not directly correspond to the true oscillation amplitude of the ions. Instead, the measured ESM amplitude is a mechanically amplified response of the pure

https://doi.org/10.1021/acs.jpcc.6c01404
J. Phys. Chem. C XXXX, XXX, XXX−XXX

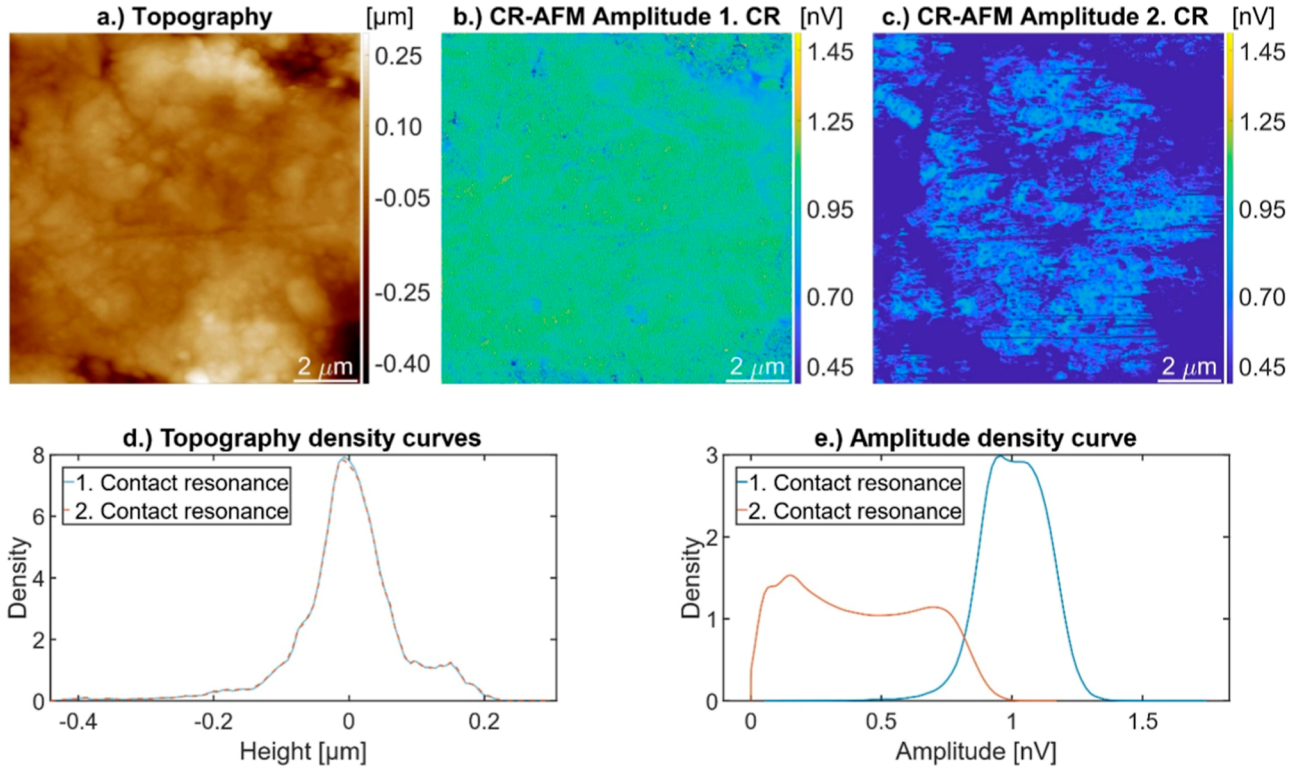


Figure 3. (A) Topography of the NCM622 particle, (b) amplitude at the first contact resonance (CR) recorded in the region shown in (a), and (c) amplitude at the second CR at the corresponding position, in (d) The histogram of the topography for both images is shown, in (e) the corresponding amplitude of (b) and (c) are shown.

ionic displacement, and the amplification is affected by the mechanical influence of k_{eff}. In the context of mechanical measurements, however, this scenario is fundamentally different as the measured amplitude is derived directly from the interaction forces, thereby signifying a genuine dynamic interplay between the tip and the sample.

Experimental Validation

To measure the mechanical properties and validate the theoretical prediction that by measuring at the resonances a part of the ESM signal has a mechanical origin and not only an ionic contribution in a first step the pure mechanics are measured with CR on an NCM622 sample.

Figure 3a, displays the topography of the NCM622 particles. These large particles appear as round-shaped agglomerates with an average diameter of approximately 7 μm. Figure 3b depicts the amplitude at the first contact resonance, which was recorded simultaneously. The signal appears largely homogeneous across the field of view, which hinders reliable identification of individual particles and is consistent with the corresponding topography. Adjustments to the color scale range do not enhance contrast or improve feature discrimination. In the image acquired at the first resonance frequency, the response remains nearly uniform, with only a faint, approximately circular region of slightly increased intensity that may indicate the presence of a particle. This is changed in Figure 3c, showing the 2. CR amplitude, where the particle appears as a lighter blue structure. Unlike in (a), where the contrast is purely topographic, the contrast in (b and c) arises from mechanical property variations, thereby enhancing the distinction between particles and the surrounding binder material. As illustrated in Figure 3c the outer region of the particle agglomerates exhibits a higher amplitude than the inner core of the particles, which seems to have a kind of hole in the middle. This has already been reported and discussed in an earlier publication.[8] A close comparison of Figure 3(a,b) reveals that the contrast of only the first CR amplitude does not always reveal the exact position of individual particles in the material. It is only through the utilization of mechanical contrast, as exhibited by the second CR, that a clear imaging of the particles can be achieved. The histogram in Figure 3d shows identical topographies and thus verifies that both images were recorded at the identical position and that the topography is independent of whether probed at the first and second eigenmode.

As expected, a comparison between Figure 3(b,c) reveals a change in the amplitude and intensity of the particles, as shown in the density plot in Figure 3(e). As shown in Figure 3, the amplitude of the first contact resonance is higher on the NCM particles. A similar behavior is observed for the second contact resonance, where the particle regions likewise exhibit increased amplitudes. At first glance, this appears to contradict eq 4, which predicts that the amplitude scales inversely with the square root of the effective stiffness $A \propto \frac{1}{\sqrt{k_{\text{eff}}}}$, suggesting a reduced oscillation amplitude for the stiffer ceramic particles compared to the softer polymer phase. However, this relationship is only valid under the assumption of constant damping. In reality, the polymer binder exhibits significantly higher viscoelastic losses, leading to an increased damping coefficient. Since the resonance amplitude scales inversely with the damping term at resonance $A \propto \frac{1}{\gamma_n}$, variations in energy dissipation dominate the amplitude contrast. Consequently, the lower damping of the ceramic particles results in higher measured amplitudes despite their increased stiffness. It is

https://doi.org/10.1021/acs.jpcc.6c01404
J. Phys. Chem. C XXXX, XXX, XXX−XXX

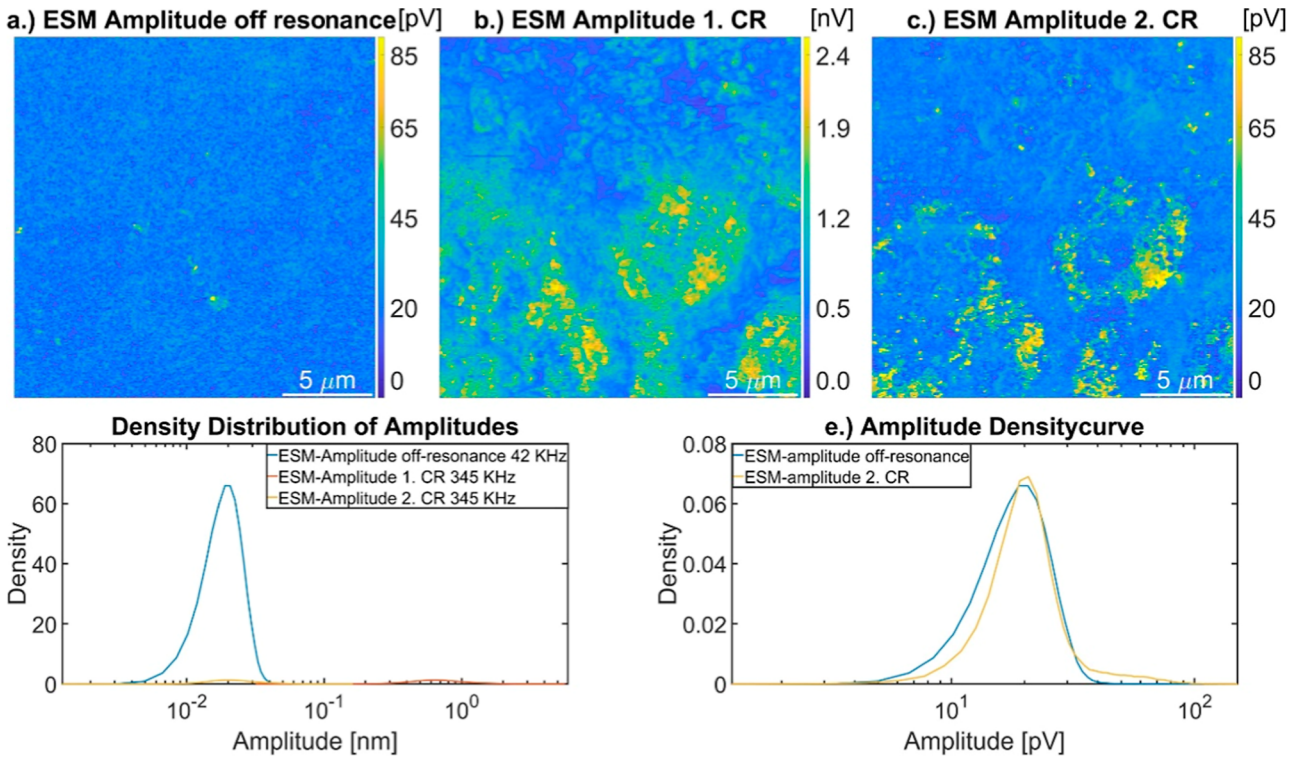


Figure 4. (A) shows the ESM amplitude at 42 kHz (off-resonance), (b) at the first contact resonance (CR) around 340 kHz, and (c) at the second CR around 1 MHz (d) displays the amplitude histograms for all three cases, while (e) compares the histograms for only the off-resonance and the 2. CR.

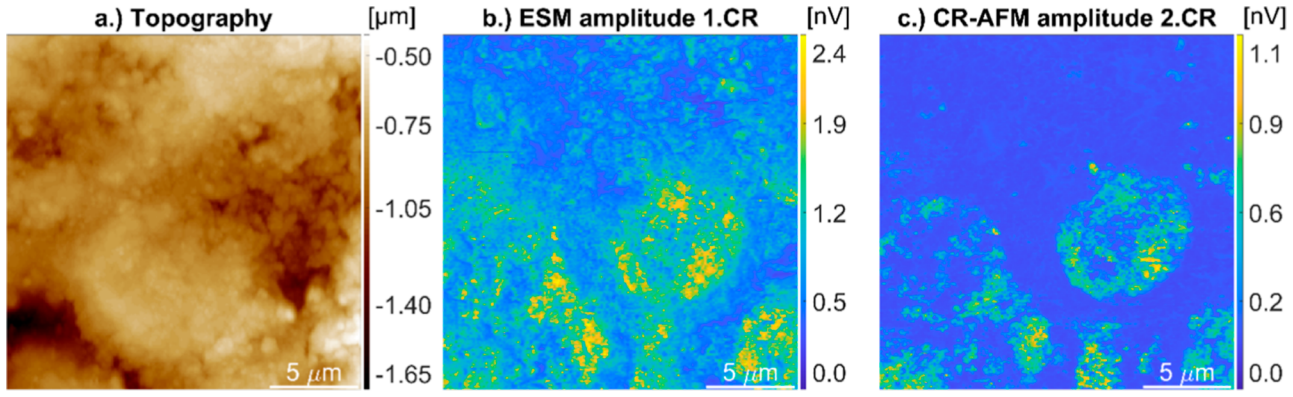


Figure 5. (A.) Topography of the NCM622 particle, (b) amplitude at the first contact resonance (CR) recorded in the region shown in (a), and (c) amplitude at the second CR at the corresponding position.

shown from the data presented in Figure 3 that an increase in the eigenmodes of the contact resonance leads to an increase in the mode-dependent stiffness of the cantilever, as this stiffness is a frequency-dependent variable, that increases with higher mode number.[33] This, in turn, results in an increase in the effective spring constant, according to eq 2. When considered in addition to the inverse proportionality of the amplitude, a decline in amplitude can be deduced. This effect is also shown by comparing Figure 3(e). The amplitude density curves exhibit the same characteristic multipeak structure, indicating a comparable underlying response for both contact resonances. In both distributions, three characteristic peak regions can be identified: a low-amplitude peak, an intermediate shoulder-like contribution, and a dominant high-density maximum. While these features occur at different absolute amplitudes, their relative arrangement remains consistent. Compared to the second contact resonance, the first contact resonance appears compressed along the amplitude axis, resulting in a narrower distribution in which the individual peak positions are shifted closer together. Thus, the primary difference between both curves is not the peak topology but the reduced amplitude span of the first contact resonance.

Electrochemical Strain Microscopy

In this section, ESM is applied to measure the ionic contribution. Figure 4 illustrates the ESM amplitude at three different frequencies at an identical sample position. The corresponding topography is presented in Figure 5(a). In contrast to the experimental setups underlying the results in Figure 3, no photothermal excitation is employed in this experiment. Figure 4(a) shows the ESM amplitude at a fixed

https://doi.org/10.1021/acs.jpcc.6c01404
J. Phys. Chem. C XXXX, XXX, XXX−XXX

frequency far away from the 1. CR frequency (42 kHz), hence off resonance. Only a limited number of pixels exhibit a measurable ESM signal above the noise level. The remaining part of the sample has a signal close to zero at this particular frequency. In Figure 4(b), the first eigenmode (approximately 345 kHz) demonstrates enhanced contrast of the particles, particularly in comparison with the mechanical data presented in Figure 3(b). The round particle located near the center of the image is clearly visible due to the increased amplitude. The phenomenon with an increased signal at the rim of the particle and lower amplitude is also observed. As illustrated in Figure 4(c), an increase in the frequency to the second eigenmode (~1 MHz) shows enhanced contrast and signal amplification, as similarly observed in the mechanical measurements Figure 3(c). However, compared to the first eigenmode image, a loss of signal intensity at some regions is detected.

In the low-frequency regime depicted in Figure 4(a), it is hypothesized that the amplitude originates exclusively from ionic motion induced by the AC bias. As the signal is not measured at the resonance, no amplification of the amplitude occurs. Here, it is expected to have the strongest unamplified amplitude, because of the drop of the Vegard coefficient with increasing frequency $f^{-1/3}$. The expected frequencies with the strongest unamplified amplitudes are below 50 kHz.[34,35] The drop of the Vegard coefficient at higher frequency leads to smaller amplitudes as shown in eq 6. However, the sufficiency of this frequency regime to facilitate the ionic movement of ions remains a subject of debate. The original idea to compensate this drop in the amplitude is the resonance enhancement. Consequently, the mechanical enhancement that is based on the sample properties is being negated. Nevertheless, ionic motion is subject to significant constraints imposed by the diffusion rate within the solid medium. Due to the limitation of the diffusion speed the contribution of the ionic motion is predominant at frequencies within the range of a few Hz to a few kHz.[5] However, at this stage it cannot be fully excluded that no detectable ESM signal is present. In conclusion, at 1 MHz (as illustrated in Figure c), it is physically implausible for the ions to follow the excitation frequency. But since a clear signal is observed, there needs to be another force interacting with the probe. The finding that at 1 MHz an amplitude is still measured, indicates that an alternative mechanism to the established classical ESM mechanism might be accountable for exciting the cantilever at higher frequencies. In accordance with the principles of ESM theory,[36] an increase in the ESM amplitude is anticipated as a consequence of cantilever resonance. However, as demonstrated in eq 6, such an enhancement can be problematic due to its susceptibility to any other force influence.

Comparison Between CR-AFM and ESM

A visual comparison reveals a striking similarity between the CR, Figure 3, and ESM amplitude maps, Figure 4, that are measured on identical positions. This suggests a strong correlation between the local mechanical response and either the ionic concentration or mobility. An alternative interpretation to the original assumptions is that the ESM signal exhibits pronounced coupling to the sample's mechanical properties. A comparison between ESM and CR-AFM signals, as direct quantitative comparison is inherently challenging due to the fundamentally different amplitude scales and transfer functions of the two techniques. A meaningful quantitative comparison would require evaluating both signals at identical excitation frequencies. However, as shown in Figure 4c of the manuscript, the second resonance does not provide an optimal signal for ESM, whereas for CR-AFM the second resonance is particularly sensitive and therefore most informative. Therefore, a more quantitative analyses based on normalization of each data set does not provide any additional insight. To further clarify this relationship, a visual comparison of the second eigenmodes of CR-AFM and the first eigenmode of CR-AFM is presented in the following section.

As shown in Figure 5(a), the zoomed-in topography of another NCM622 particle reveals small crystallites. The overall surface morphology is similar to that observed in Figure 3(a). However, no pronounced height variations are detected in this specific region of interest, whereas Figure 5(a) exhibits a more distinct topographical contrast.

Figure 5(b,c) present the amplitudes of the first contact resonance (ESM) and the second contact resonance (CR), respectively. A comparison of the amplitude images reveals clear similarities, the round particles are in both images clearly recognizable. The ESM detects a bit more signal, outside the particle, so in the binder regime, but this could be based on a softer eigenmode which is more sensitive to the softer polymer. But overall, all important features are detectable in both different amplitude images.

Based on the findings in this study, it can be postulated that a strong correlation exists between the mechanical response and the anticipated ESM response. Considering the physical parameters associated with the diffusion limit of ions, like ionic mass, lattice parameter, lithium exhibits a diffusion rate that is insufficient for Li ions to respond to an AC signal with a frequency exceeding 1 MHz. Therefore, as obtained by the 1 MHz ESM image, the mechanical influence of the resonance condition is contributing. This finding suggests that ESM data is significantly influenced by the mechanical properties of the sample. This observation is also consistent with the marginal signal that was detected in the low frequency image in Figure 5(c), as there is nearly no signal measurable. An important question for further investigation is whether the signal at 42 kHz is intrinsically too weak to be reliably detected and would merely require additional amplification, or whether such amplification would introduce distortions and thereby lead to a misinterpretation of the underlying signal caused by the mechanical crosstalk.

DISCUSSION ENHANCEMENT MECHANISM

The measurements demonstrate an almost undetectable amplitude for the off-resonance measurement in the ESM data shown in Figure 4(a). This confirms that the ESM signal needs to be amplified to be detected. The standard ESM method of measuring at resonance shows a stronger signal, but this might be prone to mechanical crosstalk. Considering that the Vegard coefficient decreases with increasing frequencies raises the question of whether amplification by measuring at resonance, and therefore at much higher frequencies, is beneficial. Figure 3 shows a significantly higher amplitude, but it remains unclear how much of the amplified signal is based on ionic motion rather than mechanical contributions. The data presented in Figure 3 demonstrate analogous behavior to the mechanical amplitude response, whereby an increase in contrast is observed with an increase in frequency. This finding suggests a predominant mechanical contribution as opposed to a purely ionic one. However, as predicted in eq 8, the presence of an oscillation force is necessary to induce

https://doi.org/10.1021/acs.jpcc.6c01404
J. Phys. Chem. C XXXX, XXX, XXX−XXX

enhancement. If at high frequencies the ionic deformation u_{ion} approaches zero the amplitude should also approach zero. Initially, it was hypothesized that this force was generated by ionic motion; however, at 1 MHz, ionic motion cannot act as a driving force, as the diffusion is physically limited. This observation indicates the necessity of an additional driving force. Other potential sources of this driving force include thermal expansion resulting from current flow (Joule heating). However, it should be noted that such a signal would not be expected to exhibit frequency dependence and would likely lead to degradation of the binder material, a process that should be observable in the topography. No such changes are detected, as topography images recorded several hours apart remain consistent, also the histograms in Figure 3(d) reveals no differences. Another potential factor contributing to this phenomenon is the formation of static electrostatic forces on the surface area. However, as the surface was connected to ground, this should have been prevented. Therefore, the most probable source of the ESM signal is spontaneous polarization and the formation of dipoles within the frequency range under the applied AC bias. Spontaneous electrostatic force formation appears to be the key factor in cantilever motion. This motion is enhanced by the resonance condition, which is affected by the mechanical properties, and leads to a contribution of the mechanical contrast that would otherwise not be visible. The electrostatic forces that are acting between tip and sample can be described with the following formula

$$F_{el}(t) = \frac{1}{2}\frac{\partial C}{\partial z}V(t)^2 \tag{9}$$

In the case of a driving AC voltage, but in the absence of any DC bias, as it is assumed in the ESM case, the electrostatic force can be described with the following equation

$$F_{el}(t) = F_0 + F_{2\omega}(t) \tag{10}$$

$$F_0 = \frac{1}{4}\frac{\partial C}{\partial z}V_{AC}^2$$

$$F_{2\omega} = -\frac{1}{4}\frac{\partial C}{\partial z}V_{AC}^2$$

As indicated by eq 10 a driving force exists but not at the investigated frequency instead at 2ω. There is a static force constant and a dynamic acting force at 2ω for a pure AC field without and DC component. As this is comparable to the off-resonance case, it is not amplified and hence negligible. It is valid that no additional external DC bias is applied, but what was not considered that there is contact potential VV_{CPD} between tip and sample. If this is taken into account the electrostatic force changed to

$$F_{el}(t) = F_0 + F_\omega \sin(\omega t) + F_{2\omega}\cos(2\omega t) \tag{11}$$

$$\frac{\partial C}{\partial z}\left[(V_{DC,ext} - V_{CPD})^2 + \frac{1}{2}V_{AC}^2 + 2(V_{DC,ext} - V_{CPD})\right.$$
$$\left. V_{AC}\sin(\omega t) - \frac{1}{2}V_{AC}^2\cos(2\omega t)\right]$$

In this case, a driving force appears at ω even for $V_{DC,ext} = 0$. As this force occurs at resonance, it will be amplified and could be the source of the acting force at high frequencies. This principle has been proven to work by Kelvin probe measurements that used the same approach to identify the surface potential.

CONCLUSION

In this paper, it is demonstrated that the contrast ratio of the amplitude in CR-AFM and ESM is significantly influenced by the selected frequency. Consequently, this indicates that operating on resonance or on higher eigenmodes of the resonance has a considerable impact on the contrast ratio. This increase is attributable to the distinct oscillatory geometry at the resonance frequency. As demonstrated earlier, it has been established that there is an optimal location for each oscillation mode, at which point maximum sensitivity is achieved.[37] Moreover, a comparison was conducted between the ESM and CR-AFM data indicating the presence of significant crosstalk between mechanical data and ESM data. However, it is notable that ESM data exhibits stronger signals in certain regions, suggesting that additional factors beyond mere mechanical influences need to be considered. It was further demonstrated that executing ESM on the sample off-resonance but still at elevated frequency (42 kHz) does not yield comparable outcomes between mechanical and ionic responses. This suggests that the mechanical influence is predominant at the resonances and not in their periphery. This is in agreement with the principles of contact mechanics, wherein an augmentation in amplitude is only valid at the resonances. The salient difference in this case is that the ESM amplitude is not based on contact mechanics; rather, the original concept was to utilize the reinforcement of the resonance to further enhance the signal amplitude. However, the data suggest that this contributes to significant crosstalk with regard to the mechanical data, which consequently complicates the analysis of separating these signal origins from each other. From these observations, it is concluded that off resonance measurements are a suitable tool for separating the mechanically dominated response observed at the resonance frequency from the ESM response dominating at low frequencies, provided that sufficient spatial resolution is achieved. In addition, the discussion addressed the hypothesis that the signal measured in the ESM can be the result of spontaneous polarization under the applied AC. This is believed to be enhanced by electrostatic interference through resonance.

ASSOCIATED CONTENT

Data Availability Statement

The data that support the findings of this study will be published after acceptance at https://doi.org/10.26165/JUELICH-DATA/3DGSTR.

AUTHOR INFORMATION

Corresponding Author

Florian Hausen − *Institute of Energy Technologies (IET-1), Forschungszentrum Jülich GmbH, D-52428 Jülich, Germany; Institute of Physical Chemistry, RWTH Aachen University, D-52074 Aachen, Germany; Jülich Aachen Research Alliance, D-52428 Jülich, Germany;* orcid.org/0000-0001-5712-6761; Email: f.hausen@fz-juelich.de

Authors

Niklas Scheer − *Institute of Energy Technologies (IET-1), Forschungszentrum Jülich GmbH, D-52428 Jülich, Germany; Institute of Physical Chemistry, RWTH Aachen University, D-52074 Aachen, Germany*

Rüdiger-A. Eichel − *Institute of Energy Technologies (IET-1), Forschungszentrum Jülich GmbH, D-52428 Jülich, Germany;*

https://doi.org/10.1021/acs.jpcc.6c01404
J. Phys. Chem. C XXXX, XXX, XXX−XXX

Institute of Physical Chemistry, RWTH Aachen University, D-52074 Aachen, Germany; Jülich Aachen Research Alliance, D-52428 Jülich, Germany; Faculty of Mechanical Engineering, RWTH Aachen University, D-52062 Aachen, Germany; orcid.org/0000-0002-0013-6325

Complete contact information is available at: https://pubs.acs.org/10.1021/acs.jpcc.6c01404

Notes

The authors declare no competing financial interest.

■ ACKNOWLEDGMENTS

This work was conducted in the laboratories of Nina Balke's group at North Carolina State University USA. The authors gratefully acknowledge Nina Balke for highly valuable discussions and insightful input. The samples were provided by Karin Kleiner, INRS-UQTR joint research unit in Trois-Rivières, Quebec, Canada. Financial support from the Federal Ministry of Research, Technology and Space (BMFTR) within the project FestBatt2Char (13XP0433B) is gratefully acknowledged. In addition, N.S. thanks the HITEC Graduate School for financial support enabling a research stay at North Carolina State University.

■ REFERENCES

(1) Balke, N.; Kalnaus, S.; Dudney, N. J.; Daniel, C.; Jesse, S.; Kalinin, S. V. *Nano Lett.* **2012**, *12*, 3399−3403.
(2) Balke, N.; Bonnell, D.; Ginger, D. S.; Kemerink, M. *MRS Bull.* **2012**, *37*, 633−637.
(3) Jesse, S.; Kumar, A.; Arruda, T. M.; Kim, Y.; Kalinin, S. V.; Ciucci, F. *MRS Bull.* **2012**, *37*, 651−658.
(4) Jesse, S.; Balke, N.; Eliseev, E.; Tselev, A.; Dudney, N. J.; Morozovska, A. N.; Kalinin, S. V. *ACS Nano* **2011**, *5*, 9682−9695.
(5) Morozovska, A.; Eliseev, E.; Balke, N.; Kalinin, S. V. *J. Appl. Phys.* **2010**, *108*, 053712.
(6) Veelken, P. M.; Wirtz, M.; Schierholz, R.; Tempel, H.; Kungl, H.; Eichel, R.-A.; Hausen, F. *Nanomaterials* **2022**, *12*, 654.
(7) Balke, N.; Jesse, S.; Morozovska, A.; Eliseev, E.; Chung, D.; Kim, Y.; Adamczyk, L.; Garcia, R.; Dudney, N.; Kalinin, S. *Nature Nanotechnol.* **2010**, *5*, 749−754.
(8) Hausen, F.; Scheer, N.; Ying, B.; Kleiner, K. Correlation of the electronic structure and Li-ion mobility with modulus and hardness in $LiNi_{0.6}Co_{0.2}Mn_{0.2}O_2$ cathodes by combined near edge X-ray absorption finestructure spectroscopy, atomic force microscopy, and nanoindentation. *Electrochem. Sci. Adv.* **2024**, *4*, No. e2300017.
(9) Jetybayeva, A.; Schön, N.; Oh, J.; Kim, J.; Kim, H.; Park, G.; Lee, Y.-G.; Eichel, R. A.; Kleiner, K.; Hausen, F.; et al. Unraveling the State of Charge-Dependent Electronic and Ionic Structure−Property Relationships in NCM622 Cells by Multiscale Characterization. *ACS Appl. Energy Mater.* **2022**, *5*, 1731−1742.
(10) Hausen, F.; Balke, N. *Curr. Opin. Electrochem.* **2024**, *47*, 101562.
(11) Tselev, A.; Morozovska, A. N.; Udod, A.; Eliseev, E. A.; Kalinin, S. V. *Nanotechnology* **2014**, *25*, 445701.
(12) Morozovska, A.; Eliseev, E.; Kalinin, S. V. *J. Appl. Phys.* **2012**, *111*, 014114.
(13) Badur, S.; Renz, D.; Cronau, M.; Göddenhenrich, T.; Dietzel, D.; Roling, B.; Schirmeisen, A. Characterization of Vegard strain related to exceptionally fast Cu-chemical diffusion in $Cu_2Mo_6S_8$ by an advanced electrochemical strain microscopy method. *Sci. Rep.* **2021**, *11*, 18133.
(14) Schön, N.; Schierholz, R.; Jesse, S.; Yu, S.; Eichel, R.-A.; Balke, N.; Hausen, F. Signal Origin of Electrochemical Strain Microscopy and Link to Local Chemical Distribution in Solid State Electrolytes. *Small Methods* **2021**, *5*, 2001279.
(15) Lushta, V.; Bradler, S.; Roling, B.; Schirmeisen, A. *J. Appl. Phys.* **2017**, *121*, 224302.
(16) Bradler, S.; Schirmeisen, A.; Roling, B. *J. Appl. Phys.* **2018**, *123*, 035106.
(17) Marinello, F.; Pezzuolo, A.; Carmignato, S.; Savio, E.; De Chiffre, L.; Sartori, L.; Cavalli, R. *AIP Conf. Proc.* **2015**, *1667*, 020009.
(18) Stan, G.; Solares, S. D. *Beilstein J. Nanotechnol.* **2014**, *5*, 278−288.
(19) Stan, G.; Gates, R. S. *Nanotechnology* **2014**, *25*, 245702.
(20) Stan, G.; King, S. W.; Cook, R. F. *Nanotechnology* **2012**, *23*, 215703.
(21) Bhushan, B.; Fuchs, H.; Hurley, D. C. *Applied Scanning Probe Methods XI: Scanning Probe Microscopy Techniques*, Springer, Berlin, Heidelberg 2009, 97−138.
(22) Yuya, P.; Hurley, D.; Turner, J. A. *J. Appl. Phys.* **2008**, *104*, 074916.
(23) Rabe, U.; Kopycinska-Müller, M.; Hirsekorn, S. *Acoustic scanning probe microscopy*; Springer, 2012; pp 123−153.
(24) Arruda, T. M.; Balke, N.; Jesse, S.; Kalinin, S. V. In *Scanning Probe Microscopy for Energy Research: Materials, Devices, and Applications*; World Scientific, 2013; pp 393−454.
(25) Kleiner, K.; Murray, C. A.; Grosu, C.; Ying, B.; Winter, M.; Nagel, P.; Schuppler, S.; Merz, M. *J. Electrochem. Soc.* **2021**, *168*, 120533.
(26) Voigtländer, B.; Scanning Probe Microscopy *Atomic Force Microscopy and Scanning Tunneling Microscopy*, 2015.
(27) Proksch, R. *J. Appl. Phys.* **2015**, *118*, 072011.
(28) Ramirez-Moreno, M. A.; Gonzalez-Hernandez, S.; Ares de Parga, G. *Physica A: Statistical Mechanics and its Applications* **2021**, *565*, 125522.
(29) Li, Q.; Jesse, S.; Tselev, A.; Collins, L.; Yu, P.; Kravchenko, I.; Kalinin, S. V.; Balke, N. *ACS Nano* **2015**, *9*, 1848−1857.
(30) García, R.; Pérez, R. *Surf. Sci. Rep.* **2002**, *47*, 197−301.
(31) Sader, J. E.; White, L. *J. Appl. Phys.* **1993**, *74*, 1−9.
(32) Proksch, R. *Scanning Probe Microscopy of Functional Materials: Nanoscale Imaging and Spectroscopy*; Springer, 2010; pp 125−151.
(33) Kiracofe, D.; Raman, A. *J. Appl. Phys.* **2010**, *107*.
(34) Alikin, D.; Slautin, B.; Abramov, A.; Rosato, D.; Shur, V.; Tselev, A.; Kholkin, A. *Materials* **2019**, *12*, 1416.
(35) Alikin, D.; Romanyuk, K.; Slautin, B.; Rosato, D.; Shur, V. Y.; Kholkin, A. *Nanoscale* **2018**, *10*, 2503−2511.
(36) Kalinin, S. V.; Dyck, O.; Balke, N.; Neumayer, S.; Tsai, W.-Y.; Vasudevan, R.; Lingerfelt, D.; Ahmadi, M.; Ziatdinov, M.; McDowell, M. T.; Strelcov, E. *ACS Nano* **2019**, *13*, 9735−9780.
(37) Eichhorn, A. L.; Dietz, C. Torsional and lateral eigenmode oscillations for atomic resolution imaging of HOPG in air under ambient conditions. *Sci. Rep.* **2022**, *12*, 8981.